Insight into the Metal–Support Interaction of Pt and β-MnO$_2$ in CO Oxidation

Tiantian Zhang [1], Jiacheng Xu [1,2], Yan Sun [1], Shiyu Fang [1], Zuliang Wu [1,3], Erhao Gao [1,3], Jiali Zhu [1,3], Wei Wang [1,3], Shuiliang Yao [1,2,3,*] and Jing Li [1,3,*]

[1] School of Environmental Science and Engineering, Changzhou University, Changzhou 213164, China; yansun.123@foxmail.com (Y.S.)

[2] School of Material Science and Engineering, Changzhou University, Changzhou 213164, China

[3] Key Laboratory of Advanced Plasma Catalysis Engineering for China Petrochemical Industry, Changzhou 213164, China

[*] Correspondence: yaos@cczu.edu.cn (S.Y.); lijing_831@cczu.edu.cn (J.L.)

Abstract: Pt-based catalysts exhibit unique catalytic properties in many chemical reactions. In particular, metal–support interactions (MSI) greatly improve catalytic activity. However, the current MSI mechanism between platinum (Pt) and the support is not clear enough. In this paper, the interaction of 1 wt% Pt nanoparticles (NPs) on β-MnO$_2$ in carbon monoxide (CO) oxidation was studied. The Pt on β-MnO$_2$ inhibited CO oxidation below 210 °C but promoted it above 210 °C. A Pt/β-MnO$_2$ catalyst contains more Pt^{4+} and less Pt^{2+}. The results of operando DRIFTS-MS show that surface-terminal-type oxygen (M=O) plays an important role in CO oxidation. When the temperature was below 210 °C, Mn=O consumption on Pt/β-MnO$_2$ was less than β-MnO$_2$ due to Pt^{4+} inhibition on CO oxidation. When the temperature was above 210 °C, Pt^{4+} was reduced to Pt^{2+}, and Mn=O consumption due to CO oxidation was greater than β-MnO$_2$. The interaction of Pt and β-MnO$_2$ is proposed.

Keywords: metal–support interaction; CO oxidation; terminal-type oxygen; bridge-type oxygen; Pt; MnO$_2$

1. Introduction

CO is a colorless, odorless, but toxic, gas [1]. CO is mainly emitted from vehicle combustion and industrial processes [2,3]. It is not only hazardous to human health, but also indirectly contributes to global warming [4]. Catalytic oxidation technology is a considerably effective method for reducing CO emission because it has high economic feasibility, lower cost, and lower secondary pollution generation [5]. Transition metal oxide catalysts have shown promising applications due to their low cost and good poisoning and sintering resistance [6]. MnO$_2$ is widely used in catalytic oxidation reactions due to its variable valence states and good oxygen-storage and oxygen-release capacities [7–9]. MnO$_2$ can form a variety of crystal structures, such as α-, β-, γ-, and δ-MnO$_2$, according to [MnO$_6$] as a backbone arrangement [7]. Among them, β-MnO$_2$ has a thermodynamically stable phase and high crystallinity, which has become one of the current research hotspots [10]. It is still a challenge for MnO$_2$ to perform CO oxidation at low temperatures [11,12].

Loading a noble metal onto a support is an effective way to improve catalytic activity. Noble metal–supported catalysts have been widely used in CO oxidation due to the MSI [2]. Among them, platinum (Pt)-based catalysts have attracted wide attention for their excellent catalytic activity [13]. Zhu et al. used a Pt/Al$_2$O$_3$ catalyst to convert formaldehyde at room temperature [14]. Huang et al. prepared a Pt/CeO$_2$-TiO$_2$ catalyst and found that it has high catalytic activity and selectivity for CO + NO reactions [15]. Cui et al. prepared an octahedral Fe$_3$O$_4$ to support Pt to remove formaldehyde and found that the catalyst has a high activity and stability [16]. Ru et al. synthesized Pt/(α-, γ-, and δ-) MnO$_2$ catalysts for

methanol oxidation, and showed that the temperatures for methanol oxidation on Pt/(α-, γ-, and δ-) MnO_2 catalysts can be reduced in comparison with MnO_2 [17].

MnO_2 has two typical oxygen species: terminal-type oxygen (Mn=O) and bridge-type oxygen (Mn-O-Mn) [18]. Mn=O plays an important role in the CO oxidation process [19]. MSI can inhibit the growth of small noble metal nanoparticles and optimize the bonding structure and electron transfer, and, thus, improve catalytic performance [13]. Dispersion of Pt NPs onto MnO_2 is an efficient method to weaken Mn=O and Mn-O-Mn bonds and generate oxygen vacancies through MSI between interfaces of Pt NPs and MnO_2 [20]. However, some studies have shown that the strong interactions may limit catalytic reactions and weaken catalytic activity [13]. Miao et al. found that excessively strong MSI does not promote O_2 adsorption [13,21]. At present, the interaction between Pt and the support is not clear enough. This study aims to gain insight into the interaction of Pt and MnO_2 in CO oxidation.

Operando diffuse reflectance infrared Fourier transform spectroscopy (DRIFTS) can monitor surface species and oxygen vacancies under a real reaction condition and is often used to study catalytic reaction mechanisms [10]. Xu et al. used H_2 as a probe molecule to study the role of oxygen species on the surface oxygen species of β-MnO_2 of a low amount of M=O using operando DRIFTS coupled with mass spectrometry (MS) [10]. Li et al. studied the effects of acid gases (NO, HCl, and SO_2) on mercury oxidation over CeO_2-WO_3/TiO_2 catalysts through in situ DRIFTS and showed that NO_2 and nitrate are active centers of mercury oxidation [22]. Using CO as a probe molecule and in situ DRIFTS, Jang et al. quantified a part of the catalytic active sites on PdOx, further elucidating the surface reconstruction of Pt-Pd bimetallic particles during the reaction [23]. Zhang et al. confirmed that Rh atoms are dispersed on Al_2O_3 and TiO_2 using Fourier transform infrared spectroscopy (FTIR) [24].

In this study, 1 wt% Pt NPs loaded on β-MnO_2 prepared with deposition–precipitation is used to explore the metal–support interaction of Pt and β-MnO_2 during CO oxidation. The physicochemical properties of β-MnO_2 and Pt/MnO_2 catalysts are characterized using an X-ray diffractometer (XRD), high-resolution transmission microscopy (HRTEM), X-ray photoelectron spectroscopy (XPS), and paramagnetic resonance spectroscopy (EPR). The role of oxygen species on the surfaces of β-MnO_2 and Pt/β-MnO_2 catalysts in CO oxidation is revealed using operando DRIFTS-MS. The interaction of Pt and β-MnO_2 in CO oxidation is proposed.

2. Results and Discussion

2.1. Physical Phase Characterization

Figure 1 shows the XRD patterns of two catalysts. The diffraction peaks of β-MnO_2 correspond to JCPDS 24-0735, and 2θ = 28.7°, 37.4°, 42.8°, 56.7°, and 59.5° correspond to (110), (101), (111), (211), and (220) crystal planes, respectively. β-MnO_2 exhibits sharp and narrow diffraction peaks, suggesting that β-MnO_2 has a high degree of crystallinity [25]. No diffraction peaks of Pt have been observed from XRD patterns, which may be due to small particle size, low Pt loading, or high dispersion of the Pt NPs [13,26–29]. The positions of the diffraction peaks of Pt/β-MnO_2 are consistent with that of β-MnO_2, indicating that the loading Pt did not change the crystal structure of β-MnO_2. However, after loading Pt, the intensities of the diffraction peaks decreased, indicating that the crystallinity of β-MnO_2 can be affected by Pt loading [30].
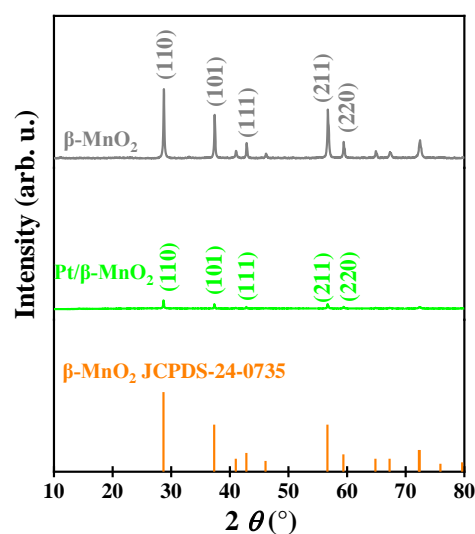
Figure 1. XRD patterns.

Figure 2 shows the HRTEM images of the two catalysts. The lattice spacing of β-MnO$_2$ is 0.311 nm (Figure 2a), which is consistent with the (110) crystal face of β-MnO$_2$. After loading Pt on β-MnO$_2$, it was found that there are some crystal-plane blurs between the normal lattice stripes (inside the red circles in Figure 2b). This fact implied that the loading of Pt NPs caused defects in the catalyst [31]. Although no crystal planes of Pt species were observed in HRTEM, the presence of Pt NPs could be confirmed from HRTEM images (Figure 2c,d). The sizes of the Pt NPs were between 1.0 and 2.0 nm.
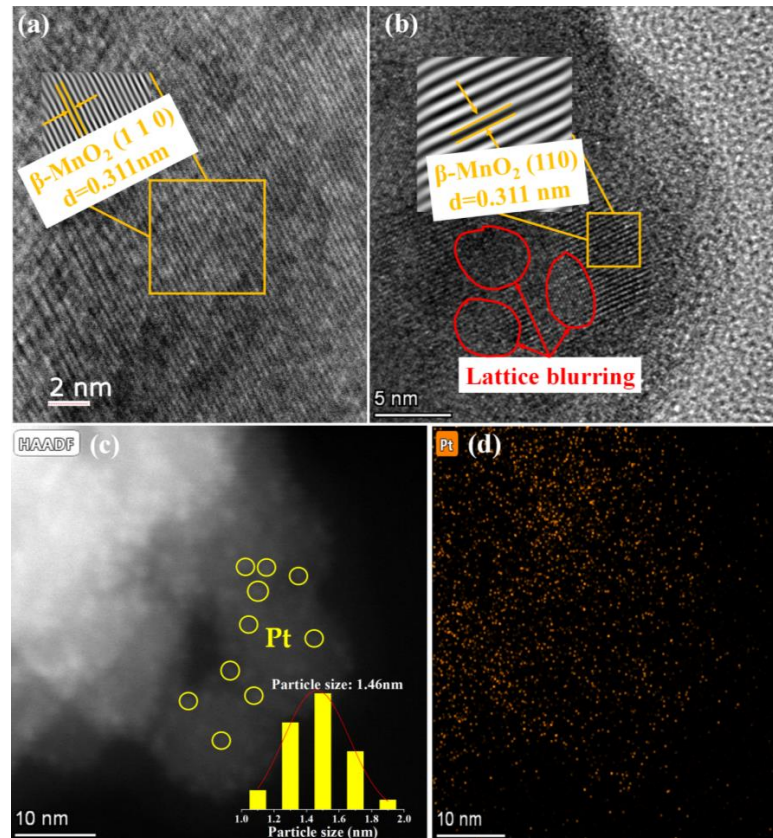

Figure 2. HRTEM images. (**a**) β-MnO$_2$; (**b**) and (**c**) Pt/β-MnO$_2$; (**d**) mapping of Pt on Pt/β-MnO$_2$.

The N_2 adsorption isotherm and pore-size distribution curves of the two catalysts are shown in Figure 3. The physical and chemical properties of the two catalysts are summarized in Table 1. According to the IUPAC classification, the N_2 adsorption isotherms of both catalysts are type IV isotherms. The specific surfaces before and after Pt loading are the same. However, the BJH pore-size distribution showed that β-MnO$_2$ mainly has a microporous structure (<2 nm), while Pt/β-MnO$_2$ is mainly of a mesoporous structure (2–50 nm). After loading Pt NPs, the pore volume of β-MnO$_2$ decreased and the pore diameter increased, indicating that the small pores in β-MnO$_2$ were blocked by Pt NPs.
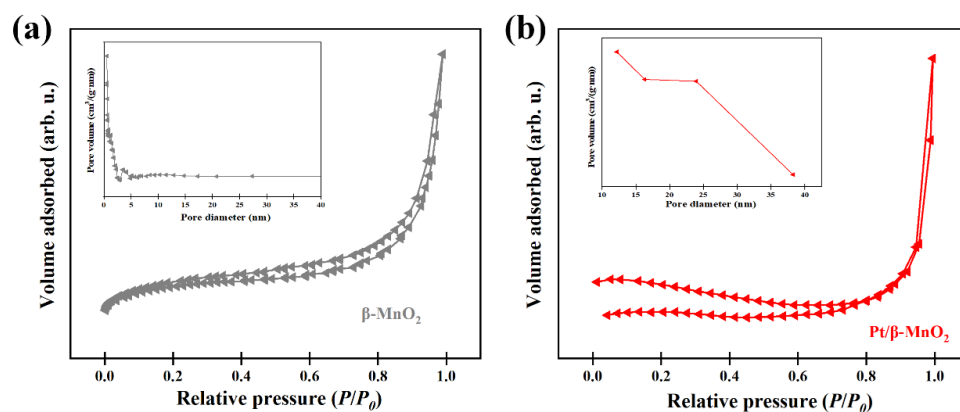

Figure 3. N_2 adsorption/desorption isotherms and pore size distributions. (**a**) β-MnO$_2$ and (**b**) Pt/β-MnO$_2$.

Table 1. Specific surface areas, pore volumes, and pore diameters.

Catalyst	β-MnO$_2$	Pt/β-MnO$_2$
BET surface (m^2 g^{-1})	1.29	1.29
Pore volume (cm^3 g^{-1})	0.00354	0.00174
Pore diameter (nm)	5.83	32.74
T_{10} (°C)	140	182
T_{50} (°C)	235	212
T_{90} (°C)	310	222

2.2. Catalytic Activity

The catalytic activities of the two catalysts are shown in Table 1 and Figure 4. Pt/β-MnO$_2$ has T_{50} and T_{90} values, lower than β-MnO$_2$. This means that loading Pt can enhance the activity of β-MnO$_2$. The *TOF* value of Pt/β-MnO$_2$ at 222 °C (T_{90}) was 0.06 s^{-1}; this *TOF* value is around the order of Pt NPs on SiO$_2$ [32].
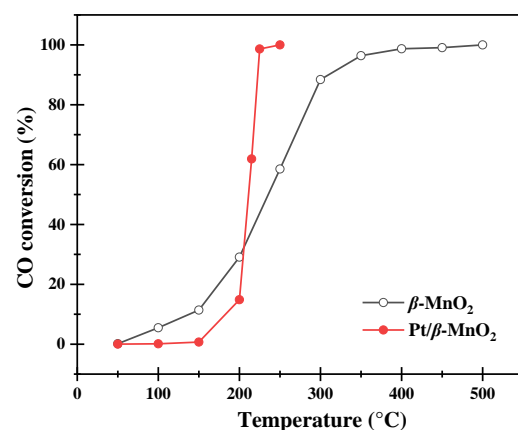
Figure 4. CO conversion at various temperatures.

It should be noted that CO oxidation on Pt/β-MnO$_2$ is lower than that of β-MnO$_2$ at a temperature below 210 °C. This result suggested that Pt NPs inhibited CO oxidation below 210 °C by Pt NPs alone or in combination with β-MnO$_2$. The inhibition mechanism is discussed later in Section 3.

2.3. Surface Chemical Structures

The surface chemical structures of the two catalysts were characterized using XPS and Raman. Figure 5 shows the XPS spectra of the two catalysts. Each element is qualitatively identified and semiquantitatively calculated using the peak areas of each element [28,29]. The results are listed in Table 2. The peaks of 641.6, 642.5, and 643.6 eV (Figure 5a) correspond to Mn^{2+}, Mn^{3+}, and Mn^{4+}, respectively [10]. The peak-area ratios of Mn cations with different valence states are shown in Table 2. Before and after Pt loading, the (Mn^{2+} + Mn^{3+})/Mn^{4+} ratio increased from 3.55 to 4.00, proving that Pt NPs on β-MnO$_2$ can promote the formation of Mn^{2+} and Mn^{3+}; those contribute to the formation of oxygen vacancies [33]. Moreover, the increase in the Mn^{2+} and Mn^{3+} ratio is also related to the formation of Pt-O-Mn [20].
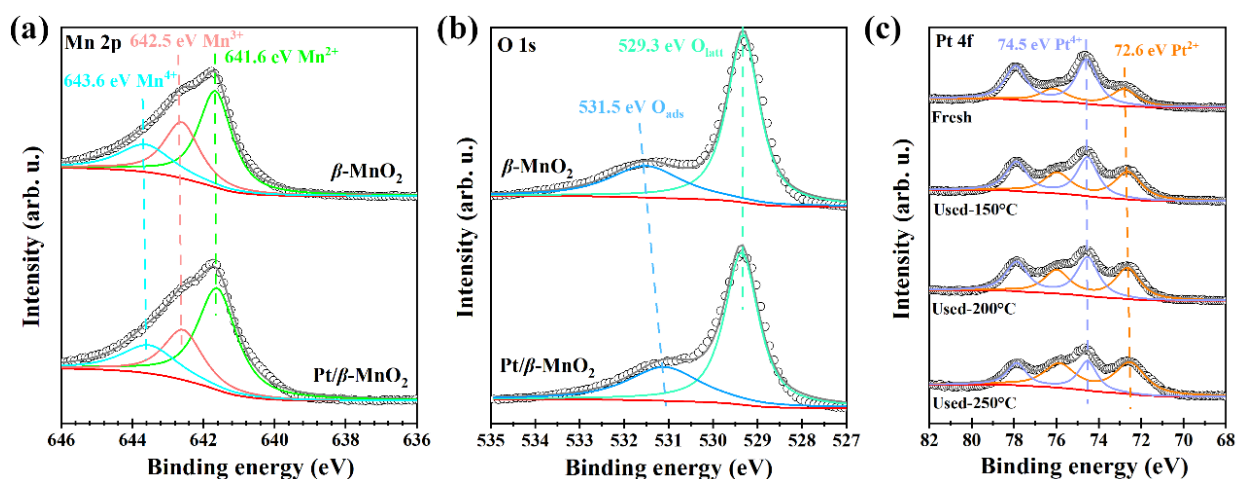

Figure 5. XPS spectra. (**a**) Mn 2p; (**b**) O 1s; and (**c**) Pt 4f.

Table 2. XPS and Raman analysis results.

Catalyst	XPS				Raman
	(Mn^{2+} + Mn^{3+})/Mn^{4+}	O$_{ads}$/O$_{total}$	Pt^{2+}/Pt$_{total}$	Pt^{4+}/Pt$_{total}$	Mn=O Ratio *
β-MnO$_2$	3.55	0.30			0.45
Pt/β-MnO$_2$-fersh	4.00	0.33	0.32	0.68	0.66
Pt/β-MnO$_2$-used-150 °C **			0.48	0.52	
Pt/β-MnO$_2$-used-200 °C **			0.51	0.49	
Pt/β-MnO$_2$-used-250 °C **			0.64	0.36	

* Mn=O ratio: M=O/(M=O + M-O-M). ** Pt/β-MnO$_2$ catalysts after CO oxidation in 1% CO/20%/N$_2$ atmosphere at 150 °C, 200 °C, and 250 °C for 1 h, respectively.

The XPS spectra of O1s are shown in Figure 5b. The peaks at 529.3 and 531.5 eV correspond to lattice oxygen (O$_{latt}$) and surface-adsorbed oxygen (O$_{ads}$), respectively [10]. The peak-area ratios of the surface oxygen species on the two catalysts are listed in Table 2. The O$_{ads}$/(O$_{ads}$ + O$_{latt}$) ratios of β-MnO$_2$ and Pt/β-MnO$_2$ are 0.30 and 0.33, respectively. Pt/β-MnO$_2$ has more adsorbed oxygen than β-MnO$_2$, which supports the fact that a higher (Mn^{2+} + Mn^{3+})/Mn^{4+} ratio can generate more oxygen vacancies on Pt/β-MnO$_2$. The more surface-adsorbed oxygen is essential for catalytic oxidation [13]. Our finding also confirmed that catalysts containing more surface-adsorbed oxygen have better catalytic activity (Figure 4a). The XPS spectra of Pt 4f have broad peaks in the Pt 4f region (Figure 5c),

indicating that Pt has different valence states. The peaks of 72.6 and 74.5 eV correspond to Pt^{2+} and Pt^{4+}, respectively [13,20]. The peak-area ratios of different valence states before and after CO oxidation are given in Table 2. The Pt/β-MnO$_2$ catalyst before CO oxidation mainly has Pt^{+4} and Pt^{+2}, among which the Pt^{4+} ratio is as high as 0.68, showing that Pt^{4+} is the mainstay. The emergence of Pt^{2+} can be explained by the generation of Pt-O-Mn bonds, meaning that there is an interaction between Pt and β-MnO$_2$ [33]. After the reaction at 150, 200, and 250 °C, the ratio of Pt^{2+}/Pt_{total} gradually increased to 0.64. At the same time, the ratio of Pt^{4+}/Pt_{total} decreased to 0.36. This finding clearly explores that Pt^{4+} was continuously reduced to Pt^{2+} during CO oxidation. Since Pt^{2+} is associated with the formation of Pt-O-Mn, it is speculated that Pt-O-Mn can promote CO oxidation. Combined with the low activity of Pt/β-MnO$_2$ below 210 °C, it is concluded that Pt/β-MnO$_2$ containing more Pt^{4+} and less Pt-O-Mn is not in favor for CO oxidation.

　　　Figure 6 shows the Raman profiles of the two catalysts. The peak located in 500–700 cm^{-1} is attributed to the stretching of the [MnO$_6$] octahedron [34]. The peak around 637 cm^{-1} is the symmetrical Mn=O tensile vibration perpendicular to the [MnO$_6$] octahedral double strand. The low-intensity peak with a low wavenumber is attributed to the deformation mode of the metal–oxygen chain (Mn-O-Mn) in the MnO$_2$ octahedral lattice [35]. Compared with β-MnO$_2$, the vibration intensities of Mn=O and Mn-O-Mn after Pt loading have been weakened. This indicates that the mobility of lattice oxygen (Mn-O-Mn) increases after Pt loading [20]. The peak areas of Mn=O (A$_{Mn=O}$) and Mn-O-Mn (A$_{Mn-O-Mn}$) were calculated using LabSpec software. Pt/β-MnO$_2$ has a higher A$_{Mn=O}$/(A$_{Mn-O-Mn}$ + A$_{Mn-O}$) ratio than β-MnO$_2$ (Table 2), implying that Pt/β-MnO$_2$ has more adsorbed oxygen (Mn=O) than β-MnO$_2$.
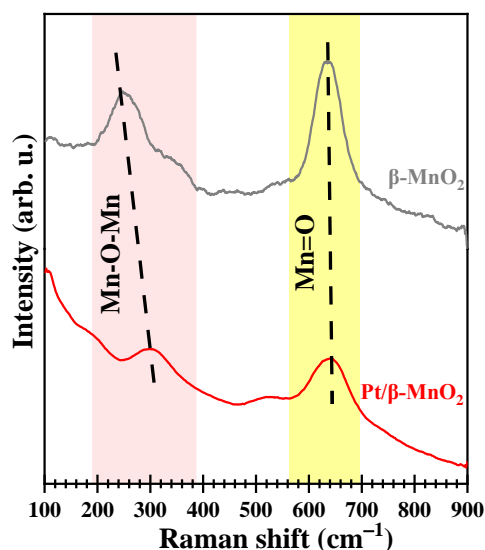

Figure 6. Raman profiles.

2.4. Reduction, Oxygen-Vacancy, and Electron-Transfer Analyses

　　　To further understand the interaction of Pt and β-MnO$_2$, H$_2$-TPR and EPR were performed. Figure 7a shows the H$_2$-TPR profiles for two catalysts. The reduction temperature can be divided into two regions, R_0 (50–200 °C) and R_I (200–600 °C). Two reduction peaks (319 and 455 °C) were observed on β-MnO$_2$, which were attributed to the reduction of Mn^{4+} to Mn^{3+} and then to Mn^{2+} [13,20]. After loading Pt, the R_0 region has the reduction peak of PtOx at 88 °C and surface-adsorbed oxygen (O$_{ads}$) at 143 °C [36]. Since the reduction peak in the R_0 region is attributed to H$_2$ spillover effects, which are caused by the formation of Pt-O-Mn bonds between β-MnO$_2$ and adjacent Pt NPs [17,37], the Pt/β-MnO$_2$ of peaks in the R_0 region interacts between Pt and β-MnO$_2$. Figure 7b shows the EPR spectra of the two catalysts. β-MnO$_2$ has obvious electron paramagnetic resonance signal peaks at g = 2.005 [36], and the peak intensity can also reflect the oxygen-vacancy concentration. After loading Pt on β-MnO$_2$, the signal at g = 2.005 is offset. This proves

that there is electron transfer between Pt NPs and β-MnO$_2$, which is consistent with typical MSI phenomena [38]. In addition, it is clear that the oxygen-vacancy concentration order is Pt/β-MnO$_2$ > β-MnO$_2$. Higher oxygen-vacancy concentrations correspond to better oxygen-mobility capacity, which is consistent with the characterization of H$_2$-TPR. The oxygen vacancies of Pt/β-MnO$_2$ increased significantly, mainly due to the fact that MSI affects the Mn=O bonds of the vector and forms more oxygen vacancies [36].
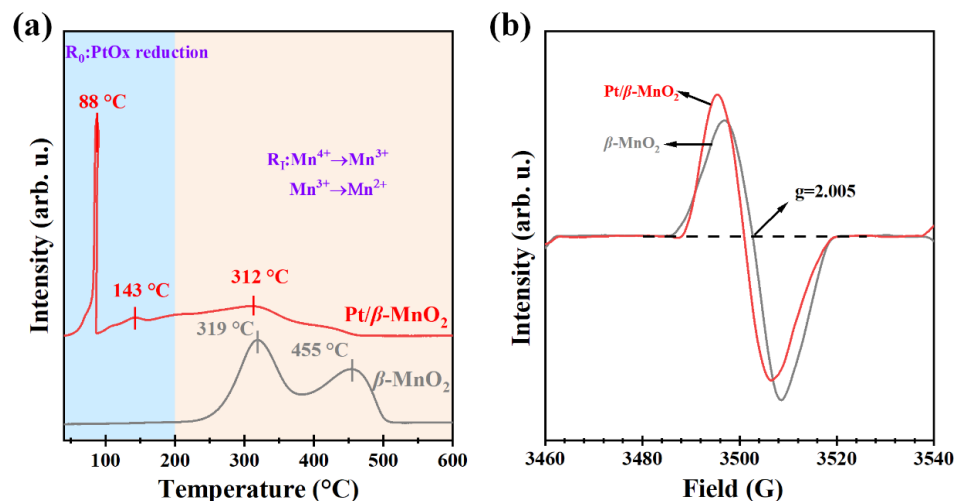

Figure 7. (**a**) H$_2$-TPR profiles and (**b**) EPR spectra.

2.5. Surface Reactions Using Operando DRIFTS-MS

2.5.1. Surface Reactions in CO Atmosphere

Figure 8 shows the operando DRIFTS spectra during CO oxidation on the two catalysts in a 1% CO/Ar atmosphere without O$_2$. The peaks on β-MnO$_2$ at 2173 and 2114 cm^{-1} belong to the gas-phase CO. On Pt/β-MnO$_2$, the peak at 2173 cm^{-1} belongs to the gas-phase CO [19], the peak at 2121 cm^{-1} belongs to CO-Pt$^{\delta+}$ [39,40], and the peak at 2068 cm^{-1} is assigned to CO-Pt^0 [39,40]. Peaks at 1300, 1112, 947, and 770 cm^{-1} are attributed to Mn=O, Mn$^+$-O$_2^-$, Mn$^+$-O$_2^{2-}$, and Mn$^+$-O^{2-}-Mn$^+$, respectively [10,19]. The peak in 1605–1688 cm^{-1} is attributed to bidentate carbonate (v(OCO)), and the peak in 1463–1560 cm^{-1} belongs to monodentate carbonate (v(CO$_3^{2-}$)) [19].
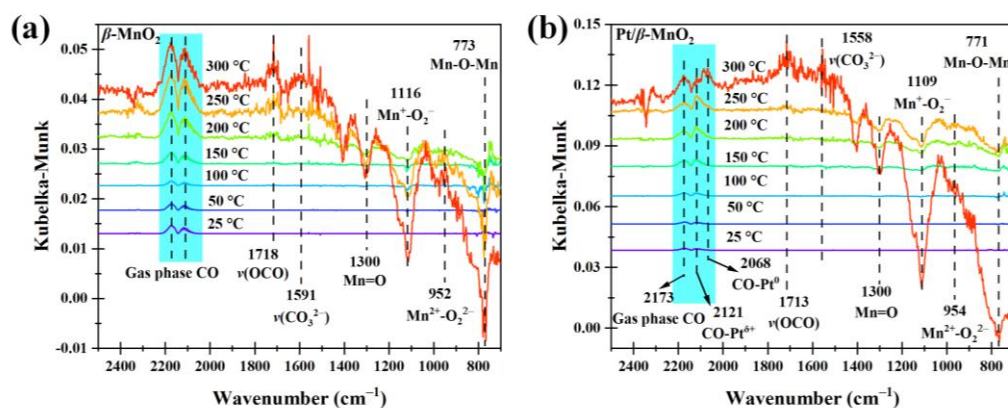

Figure 8. Operando DRIFTS spectra of two catalysts in 1% CO/Ar atmosphere. (**a**) β-MnO$_2$ and (**b**) Pt/β-MnO$_2$.

Figure 9 shows the normalized peak heights of the surface species and MS signals during CO oxidation on β-MnO$_2$ and Pt/β-MnO$_2$ in a CO atmosphere. As the temperature increased, the normalized intensities of Mn=O and Mn-O-Mn on β-MnO$_2$ and Pt/β-MnO$_2$ decreased (Figure 9a,b), indicating that oxygen species are continuously consumed due

to their reactions with CO following Equations (1)–(4). The initial consumption temperature of Mn=O on β-MnO$_2$ is 50 °C, obviously lower than that (150 °C) on Pt/β-MnO$_2$, suggesting that Mn=O on β-MnO$_2$ can react more easily with CO than that on Pt/β-MnO$_2$. This fact also implied that Pt inhibited CO oxidation by the O in Mn=O. The initial consumption temperatures of Mn-O-Mn on β-MnO$_2$ and Pt/β-MnO$_2$ are higher than 100 °C, but the normalized peak height of Mn-O-Mn on β-MnO$_2$ is less than that on Pt/β-MnO$_2$ (Figure 9b), also suggesting that Mn-O-Mn on β-MnO$_2$ can react easier with CO than that on Pt/β-MnO$_2$; Pt inhibited CO oxidation by the O in Mn-O-Mn. The reactions of Mn=O and Mn-O-Mn with CO result in the formation of Mn=$\square$ and Mn^{2+}-$\square$-Mn, where $\square$ denotes an oxygen vacancy. As the initial adsorbed O$_2$ in (O$_2{}^-$)Mn^{2+}-O-Mn is reduced to (O$_2{}^{2-}$)Mn^{2+}-$\square$-Mn by CO (Equations (5) and (6)), the decrease in the normalized peak height of (O^{2-})Mn^{2+}-O-Mn and increase in Mn^{2+}-$\square$-Mn above 50 °C (Figure 9c) proved the reactions in Equations (5) and (6). The CO oxidation products include surface carbonate and gaseous CO$_2$. Figure 9d shows the normalized peak heights of monodentate carbonate (v(CO$_3{}^{2-}$)) on β-MnO$_2$ and Pt/β-MnO$_2$. The remarkable differences between β-MnO$_2$ and Pt/β-MnO$_2$ can be found within the temperature range of 100 and 300 °C, in which the normalized peak heights of monodentate carbonate on β-MnO$_2$ are higher than that on Pt/β-MnO$_2$, indicating that Pt inhibited CO oxidation to monodentate carbonate (Equation (7)). Figure 9e illustrates no obvious difference in the normalized peak heights of bidentate carbonate on β-MnO$_2$ and Pt/β-MnO$_2$; thus, Pt has no influence on bidentate carbonate formation following Equation (9) [41].

The CO$_2$ MS signal from β-MnO$_2$ is higher than that from Pt/β-MnO$_2$ in the temperature range of 50–210 °C (Figure 9f), as Pt inhibited CO oxidation with O atoms in Mn=O and Mn-O-Mn.

$$\text{Mn=O + CO} \rightarrow \text{Mn=}\square + \text{CO}_2 \tag{1}$$

$$\text{Mn=O + CO-Pt}^{\delta+} \rightarrow \text{Mn=}\square + \text{CO}_2 \tag{2}$$

$$\text{Mn-O-Mn + CO} \rightarrow \text{Mn-}\square\text{-Mn + CO}_2 \tag{3}$$

$$\text{Mn-O-Mn + CO-Pt}^{\delta+} \rightarrow \text{Mn-}\square\text{-Mn+CO}_2 \tag{4}$$

$$(\text{O}_2{}^-)\text{Mn-O-Mn + CO}^+ \rightarrow (\text{O}_2{}^{2-})\text{Mn}^{2+}\text{-}\square\text{-Mn + CO}_2 \tag{5}$$

$$(\text{O}_2{}^-)\text{Mn-O-Mn + CO-Pt}^{\delta+} \rightarrow (\text{O}_2{}^{2-})\text{Mn}^{2+}\text{-}\square\text{-Mn + Pt}^{\delta+} + \text{CO}_2 \tag{6}$$

$$\text{Mn-O-Mn=O + CO} \rightarrow \text{Mn-}\square\text{-Mn-O-CO}_2 \tag{7}$$

$$\text{Mn=O + CO}_2 \rightarrow \text{Mn-O-CO}_2 \tag{8}$$

$$\text{Mn}^{2+}\text{-O}_2{}^{2-} + \text{CO}_2 \rightarrow \text{Mn=O}_2\text{-CO} \tag{9}$$
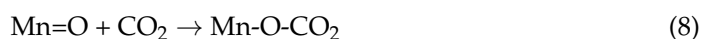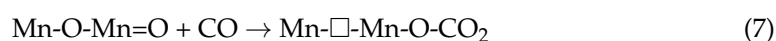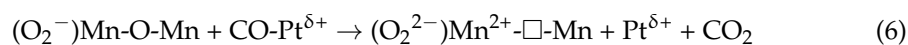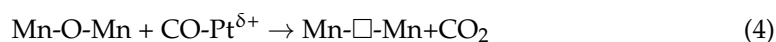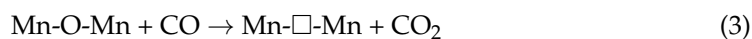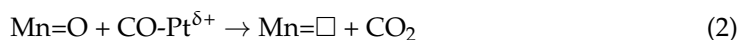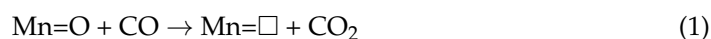
Figure 9. Normalized intensities of surface species on the surfaces of β-MnO$_2$ and Pt/β-MnO$_2$ catalysts (**a**–**e**) and MS signals (**f**) in a 1%CO/Ar atmosphere.
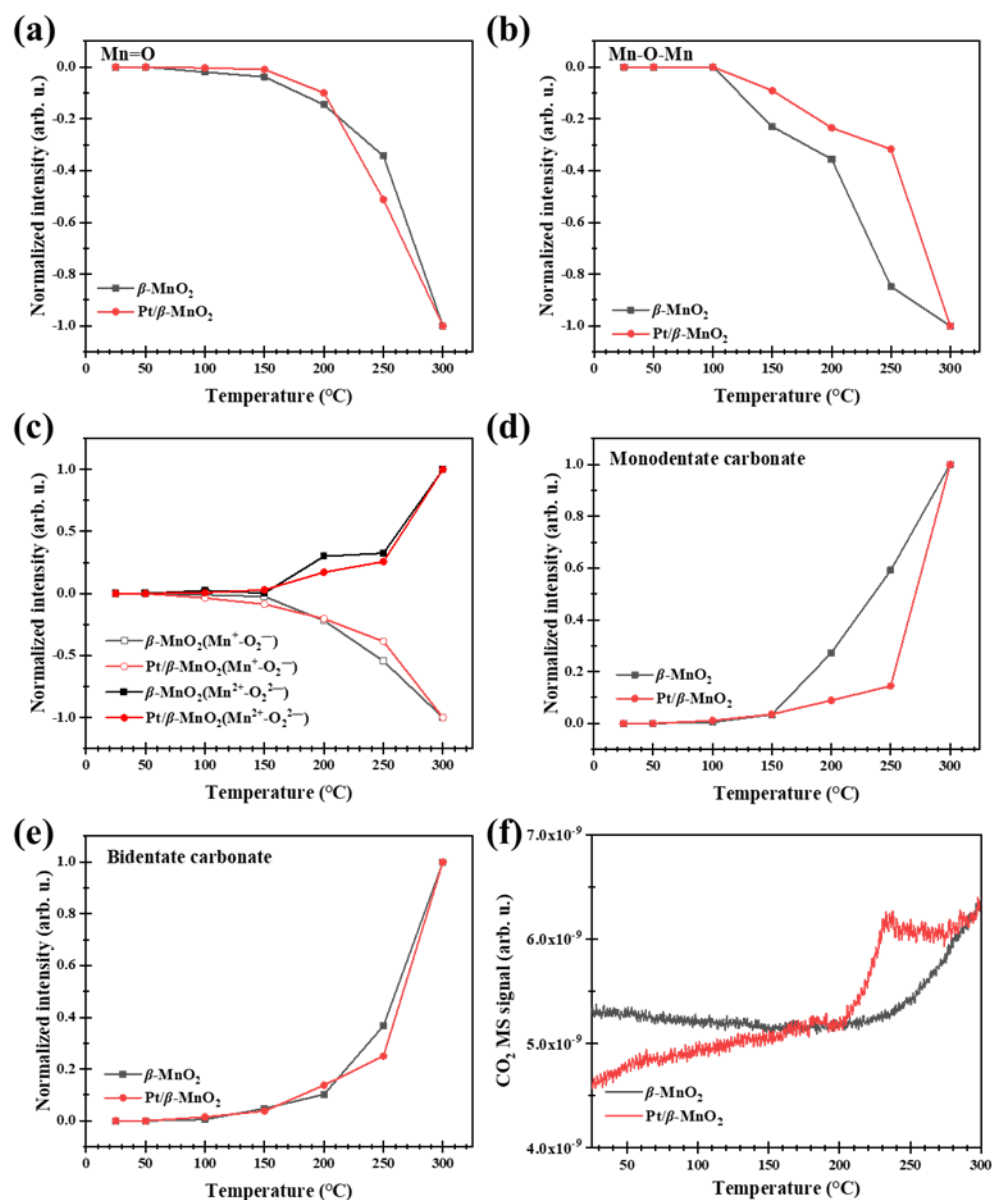
2.5.2. Surface Reactions in CO/O$_2$ Atmosphere

Figure 10 shows the DRIFTS-MS spectra of two catalysts during CO oxidation in a 1%CO/20%O$_2$/Ar atmosphere. The normalized intensities of Mn=O and Mn-O-Mn obviously decreased above 150 and 100 °C, respectively (Figure 11a,b), which are similar to those (Figure 9a,b) during CO oxidation in the absence of O$_2$. The normalized intensities of (O$_2^-$)Mn-O-Mn and Mn^{2+}-□-Mn on Pt/β-MnO$_2$ changed at 50 °C, lower than that (100 °C) on β-MnO$_2$. Since the changes of (O$_2^-$)Mn-O-Mn and Mn^{2+}-□-Mn are related to the formation of oxygen vacancy, Pt can promote the formation of oxygen vacancy in the presence of O$_2$. The normalized intensities of monodentate carbonate β-MnO$_2$ and Pt/β-MnO$_2$ (Figure 11e) are similar to those (Figure 9e), explaining that O$_2$ and Pt cannot influence the formation of monodentate carbonate.

Figure 10. Operando DRIFTS spectra of two catalysts in a 1%CO/20% O_2/Ar atmosphere. (**a**) β-MnO$_2$ and (**b**) Pt/β-MnO$_2$.
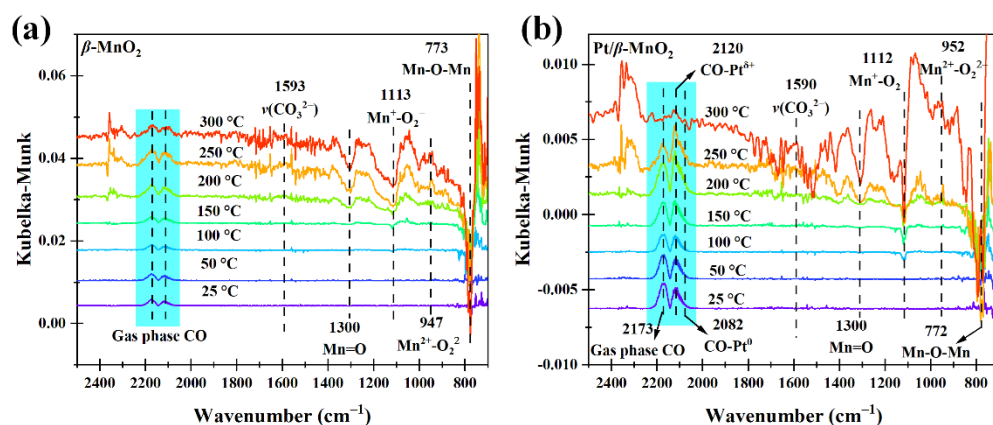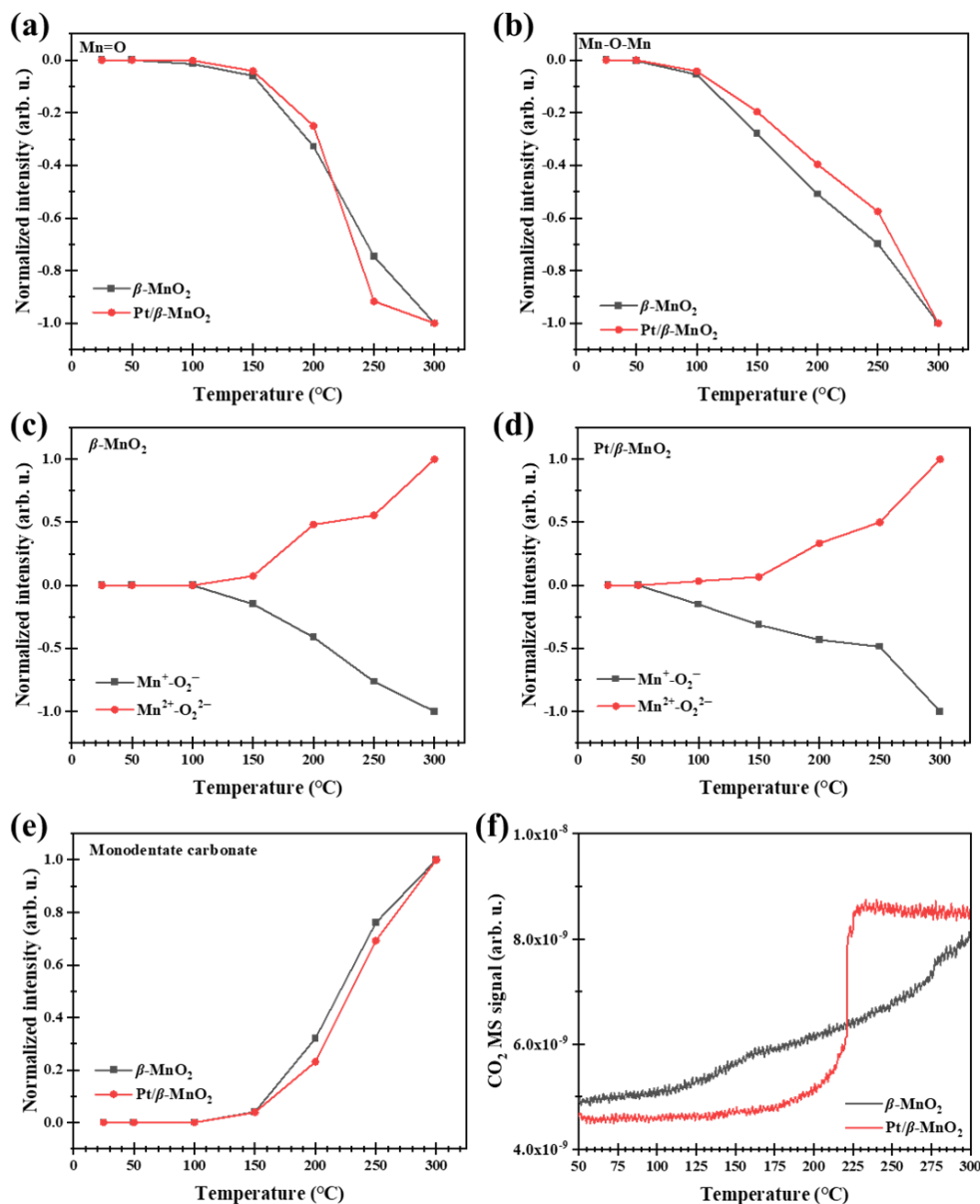

Figure 11. Normalized intensities of surface species on the surfaces of β-MnO$_2$ and Pt/β-MnO$_2$ catalysts (**a**–**e**) and MS signals (**f**) in a CO/O$_2$/Ar atmosphere.

The trend of the CO_2 MS signal (Figure 11f) is basically similar to those during CO oxidation in the absence of O_2, further proving that Pt can inhibit CO oxidation in the presence of O_2 below 225 °C. This result is consistent with that in Figure 4a.

2.5.3. Surface Reactions in O_2 Atmosphere

The normalized intensities of Mn=O and Mn-O-Mn after CO oxidation with or without O_2 are all negative (Figures 9 and 11), indicating that the regeneration rates of oxygen vacancies (Mn=□ and Mn-□-Mn) are lower than their consumption rates. To determine whether the oxygen vacancies can be regenerated, the catalysts with oxygen vacancies (generated via CO oxidation in a 1%CO/Ar atmosphere for 30 min at 300 °C) were heated from 25 °C to 300 °C with a ramp of 10 °C min^{-1} in a 20%O_2/Ar atmosphere. The regeneration results are shown in Figure 12. Figure 12a,b show the DRIFTS spectra on β-MnO_2 and Pt/β-MnO_2 during regeneration. Figure 12c,d demonstrate that the normalized intensities of Mn=O and Mn-O-Mn increased to 0 at 300 °C, indicating that O_2 decomposition at Mn=□ and Mn-□-Mn happened, resulting in the complete regeneration of Mn=O and Mn-O-Mn, where the O_2 decomposition obeys Epling–Xu mechanism (Equation (10)) [42].
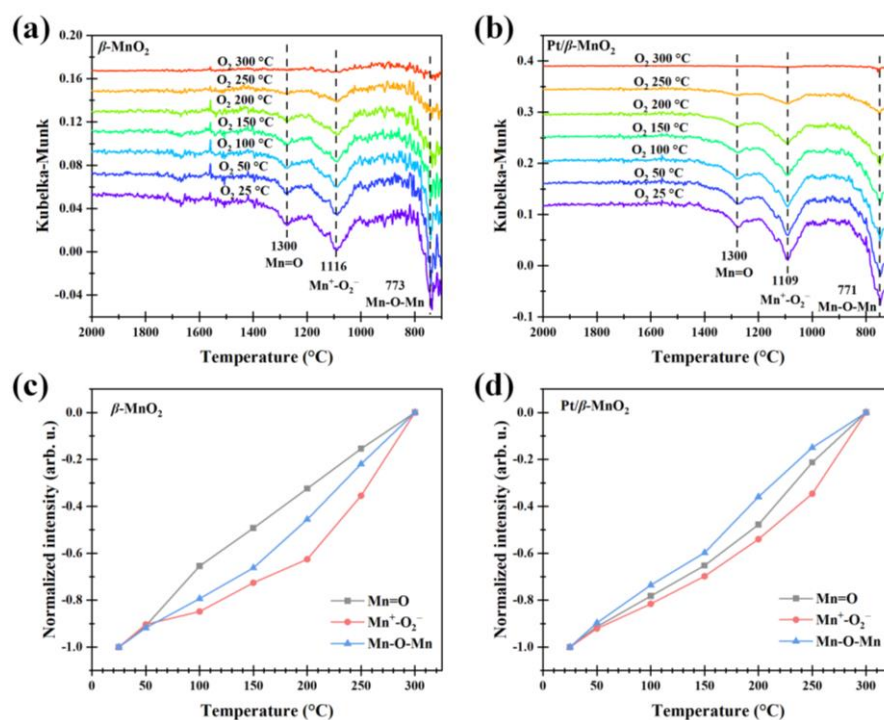
$$(O_2{}^{2-})\text{Mn-□-Mn} \rightarrow \text{O=Mn-O-Mn} \tag{10}$$

Figure 12. Operando DRIFT spectra of β-MnO_2 (**a**) and Pt/β-MnO_2 (**b**) in an O_2 atmosphere. Normalized intensities of β-MnO_2 (**c**) and Pt/β-MnO_2 (**d**).

3. Interaction of Pt and β-MnO_2 in CO Oxidation

Figure 13 shows the interaction of Pt NPs and β-MnO_2 in CO oxidation. Pt NPs are anchored on MnO_2 by Pt-O-Mn bonding, resulting in Pt^{+4} and Pt^{+2} valence states. CO is mainly adsorbed at Mn=O sites as the Pt loading is as low as 1 wt%. CO oxidation required additional O, which is from Mn=O or Pt-O-Mn and Mn-O-Mn. Step (a) indicates that O from Pt^{+4}-O-Mn is difficult, causing the inhibition of CO oxidation. Step (b) is the easy process of O supplement from Pt^{+2}-O-Mn to CO for its oxidation to CO_2. At a temperature below 210 °C, the O in Pt^{+4}-O-Mn cannot function as an O source, and Pt loading reduces the active sites of MnO_2 for CO oxidation, as Pt is anchored at places having defects. Those are active sites for CO oxidation, and this results in the inhibition of

Pt on CO oxidation. When the temperature is above 210 °C, the ratio of Pt^{+4} decreases, and the Pt^{+2} ratio increases, resulting in an increase in CO oxidation activity.
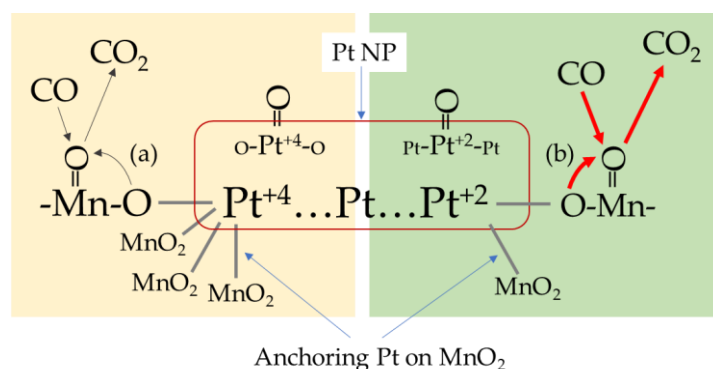
Figure 13. The interaction of Pt and β-MnO_2 in CO oxidation.

4. Materials and Methods

4.1. Catalyst Preparation

β-MnO_2 was purchased from Aladdin, Shanghai, China. Chloroauric acid ($H_2Cl_6Pt \cdot xH_2O$) was from the Shanghai McLean Company (Shanghai, China).

The 1 wt% Pt/β-MnO_2 was prepared using the deposition–precipitation method according to the method reported by Koo et al. [43]. Add $H_2Cl_6Pt \cdot xH_2O$ (0.1 g mL^{-1}), β-MnO_2 (4 g), and distilled water (100 mL) to a beaker and mix thoroughly. Place the beaker in a 60 °C water bath and stir for 1 h; $NH_3 \cdot H_2O$ was used to adjust the pH of the mixture to around 9 and then the mixture was stirred at 60 °C for 8 h. After stirring, the mixture was filtered and washed with hot distilled water and then dried at 60 °C for 12 h. After drying, the catalyst was put into a muffle furnace and calcined in an air atmosphere at 300 °C for 2 h.

4.2. Evaluation of Catalytic Activity

The CO oxidation activity of two catalysts (200 mg, 40–60 mesh) was measured in a fixed-bed flow reactor fed with 1% CO/20% O_2 balanced with N_2 at 100 mL min^{-1}, with a gas-space velocity of 60,000 mL g^{-1} h^{-1} [27]. CO and CO_2 concentrations were analyzed online using a gas chromatograph (GC9790II, Fuli, Taizhou, China) equipped with a flame ion detector with a catalyst convert to reduce CO and CO_2 to CH_4. Each catalyst was pretreated in 20% O_2 with an N_2 balance (80 mL min^{-1}) atmosphere at 300 °C for 30 min. The CO conversion (x) and turnover frequency (*TOF*, s^{-1}) were calculated using Equation (11) and Equation (12), respectively.

$$x = \frac{[CO]_{in} - [CO]_{out}}{[CO]_{in}} \times 100 \tag{11}$$

where $[CO]_{in}$ and $[CO]_{out}$ are the CO concentrations in gas streams from the inlet and outlet of the reactor, respectively.

$$TOF = \frac{F \cdot [CO]_{in} \cdot x}{m_{cat} \cdot m_{Pt}/M_{Pt}} \tag{12}$$

where F is the total gas flow rate in mol s^{-1}, m_{cat} is the amount of catalyst in g, m_{Pt} is the weight ratio of Pt in the catalyst, and M_{Pt} is the molar atomic weight of Pt (195.08).

4.3. Catalyst Characterization

The operando DRIFTS-MS was used to monitor surface species and gaseous products during CO oxidation using the method reported elsewhere [10]. The catalyst characterization was performed as per [10].

5. Conclusions

In this study, 1 wt% Pt NPs loaded on β–MnO$_2$ using deposition–precipitation was used to explore the effect of the metal–support interaction of Pt and β-MnO$_2$ in CO oxidation. The main conclusions are as follows:

(1) After loading Pt on β–MnO$_2$, it was found that Pt NPs (1–2 nm) were anchored on β-MnO$_2$ and formed Pt-O-Mn interfaces. CO oxidation was inhibited at a temperature below 210 °C and promoted above 210 °C;

(2) The ratio of Pt^{+2} dominates CO oxidation. The ratios of Pt^{+2} before the reaction and after the reaction at 150, 200, and 250 °C were Pt/β-MnO$_2$-fresh (0.32) < Pt/β-MnO$_2$-used-150 °C (0.48) < Pt/β-MnO$_2$-used-200 °C (0.51) < Pt/β-MnO$_2$-used-250 °C (0.64). Pt^{4+} can convert to Pt^{+2} by heating;

(3) The Operando DRIFTS-MS results show that Mn=O plays an important role in CO oxidation. Below 210 °C, more Mn=O was consumed on β-MnO$_2$ than on Pt/β-MnO$_2$. When the temperature is higher than 210 °C, more Mn=O was consumed on Pt/β-MnO$_2$ than on β-MnO$_2$. It is speculated that the inhibition of activity below 200 °C after Pt loading is due to Pt^{+4}, which causes less Mn=O consumption for CO oxidation;

(4) The mechanism of Pt and β-MnO$_2$ interaction is proposed, where the Pt^{+4} and Pt^{+2} functions are clearly illustrated.

Author Contributions: T.Z. Conceptualization, Investigation, Formal analysis, Methodology, Writing— original draft; J.X.: Data curation; Y.S. Data curation; S.F. Data curation. Z.W. Data curation; E.G. Validation; J.Z. Methodology; W.W. Validation; S.Y. Conceptualization, Validation; Revision, Supervision, Funding, Project administration; J.L.: Validation; Revision. All authors have read and agreed to the published version of the manuscript.

Institutional Review Board Statement: Not applicable.

Informed Consent Statement: Not applicable.

Data Availability Statement: The raw data are available from the corresponding author upon reasonable request.

Conflicts of Interest: The authors declare no conflict of interest.

Sample Availability: Samples of the compounds are not available from the authors.

References

1. Dey, S.; Mehta, N.S. Selection of Manganese oxide catalysts for catalytic oxidation of Carbon monoxide at ambient conditions. *Resour. Environ. Sustain.* **2020**, *1*, 100003. [CrossRef]
2. Wang, Y.; Zhu, L.; Li, J.; Zhang, W.; Shi, X.; Huang, Y.; Hojamberdiev, M.; Zhu, G. Metal support interaction of defective-rich CuO and Au with enhanced CO low-temperature catalytic oxidation and moisture resistance. *Adv. Powder Mater.* **2023**, *2*, 100119. [CrossRef]
3. Wu, X.; Lang, J.; Sun, Z.; Jin, F.; Hu, Y.H. Photocatalytic conversion of carbon monoxide: From pollutant removal to fuel production. *Appl. Catal. B Environ.* **2021**, *295*, 120312. [CrossRef]
4. Dey, S.; Dhal, G.C. Highly active palladium nanocatalysts for low-temperature carbon monoxide oxidation. *Polytechnica* **2020**, *3*, 1–25. [CrossRef]
5. Guo, Y.; Wen, M.; Li, G.; An, T. Recent advances in VOC elimination by catalytic oxidation technology onto various nanoparticles catalysts: A critical review. *Appl. Catal. B Environ.* **2021**, *281*, 119447. [CrossRef]
6. Guo, N.; Zhang, J.; Jiang, L.; Wang, D.; Wang, Z. Highly efficient and selective Ru and Ce modified ZSM-5 catalysts for catalytic oxidation of toluene. *Colloids Surf. A Physicochem. Eng. Asp.* **2022**, *651*, 129709. [CrossRef]
7. Chen, L.; Liu, Y.; Fang, X.; Cheng, Y. Simple strategy for the construction of oxygen vacancies on α-MnO$_2$ catalyst to improve toluene catalytic oxidation. *J. Hazard. Mater.* **2021**, *409*, 125020. [CrossRef]
8. Shi, J.; Qi, T.; Sun, B.-C.; Chu, G.-W.; Chen, J.-F. Catalytic oxidation of benzyl alcohol over MnO$_2$: Structure-activity description and reaction mechanism. *Chem. Eng. J.* **2022**, *440*, 135802. [CrossRef]

9. Gu, W.; Li, C.; Qiu, J.; Yao, J. Facile fabrication of flower-like MnO_2 hollow microspheres as high-performance catalysts for toluene oxidation. *J. Hazard. Mater.* **2021**, *408*, 124458. [CrossRef]

10. Xu, J.; Zhang, T.; Fang, S.; Li, J.; Wu, Z.; Wang, W.; Zhu, J.; Gao, E.; Yao, S. Exploring the roles of oxygen species in H_2 oxidation at β-MnO_2 surfaces using operando DRIFTS-MS. *Commun. Chem.* **2022**, *5*, 97. [CrossRef]

11. Liu, D.; Hu, F.; Yan, Y.; Ye, R.; Chen, X.; Han, B.; Lu, Z.-H.; Zhou, L.; Feng, G.; Zhang, R. Promotion of oxygen vacancies and metal-support interaction over 3DOM Au/CeO_2 catalyst for CO oxidation. *Appl. Surf. Sci.* **2023**, *629*, 157438. [CrossRef]

12. Zou, G.; Zhang, Q.; Peng, S.; She, J.; Teng, D.; Jin, C.; Che, Y. Influence of geological factors on coal permeability in the Sihe coal mine. *Int. J. Coal Sci. Technol.* **2022**, *9*, 6. [CrossRef]

13. Zhang, L.; Zhu, Z.; Tan, W.; Ji, J.; Cai, Y.; Tong, Q.; Xiong, Y.; Wan, H.; Dong, L. Thermal-Driven Optimization of the Strong Metal–Support Interaction of a Platinum–Manganese Oxide Octahedral Molecular Sieve to Promote Toluene Oxidation: Effect of the Interface Pt^{2+}–Ov–Mnδ+. *ACS Appl. Mater. Interfaces* **2022**, *14*, 56790–56800. [CrossRef]

14. Zhu, X.; Yu, J.; Jiang, C.; Cheng, B. Catalytic decomposition and mechanism of formaldehyde over Pt–Al_2O_3 molecular sieves at room temperature. *Phys. Chem. Chem. Phys.* **2017**, *19*, 6957–6963. [CrossRef] [PubMed]

15. Huang, K.; Lin, L.; Yang, K.; Dai, W.; Chen, X.; Fu, X. Promotion effect of ultraviolet light on NO+ CO reaction over Pt/TiO_2 and Pt/CeO_2–TiO_2 catalysts. *Appl. Catal. B Environ.* **2015**, *179*, 395–406. [CrossRef]

16. Cui, W.; Xue, D.; Tan, N.; Zheng, B.; Jia, M.; Zhang, W. Pt supported on octahedral Fe_3O_4 microcrystals as a catalyst for removal of formaldehyde under ambient conditions. *Chin. J. Catal.* **2018**, *39*, 1534–1542. [CrossRef]

17. Ru, X.; Li, W.; Wang, X.; Shi, Z.; Wen, X.; Mo, S.; Zhang, Q.; Mo, D. Regulating the surface local environment of MnO_2 materials via metal-support interaction in Pt/MnO_2 hetero-catalysts for boosting methanol oxidation. *Chem. Eng. Sci.* **2023**, *281*, 119079. [CrossRef]

18. Williams, O.C.; Sievers, C. Active oxygen species in heterogeneously catalyzed oxidation reactions. *Appl. Catal. A Gen.* **2021**, *614*, 118057. [CrossRef]

19. Xu, J.; Wu, Z.; Gao, E.; Zhu, J.; Yao, S.; Li, J. Revealing the role of oxygen vacancies on α-MnO_2 of different morphologies in CO oxidation using operando DRIFTS-MS. *Appl. Surf. Sci.* **2023**, *618*, 156643. [CrossRef]

20. Xie, J.; Wang, S.; Zhao, K.; Wu, M.; Wang, F. Regulating the Pt–MnO_2 Interaction and Interface for Room Temperature Formaldehyde Oxidation. *Inorg. Chem.* **2023**, *62*, 904–915. [CrossRef]

21. Miao, S.; Deng, Y. Study on total cooxidation of H_2 and CO over $Au(Pt)/Co_3O_4$ catalysts under oxygen-excessive condition. *Chin. J. Catal.* **2001**, *22*, 461–464.

22. Li, G.; Wang, S.; Wu, Q.; Li, J.; You, X.; Shao, S.; Liu, K. Exploration of reaction mechanism between acid gases and elemental mercury on the CeO_2–WO_3/TiO_2 catalyst via in situ DRIFTS. *Fuel* **2019**, *239*, 162–172. [CrossRef]

23. Jang, E.J.; Lee, J.; Oh, D.G.; Kwak, J.H. CH_4 oxidation activity in pd and Pt–Pd bimetallic catalysts: Correlation with surface PdO x quantified from the DRIFTS study. *ACS Catal.* **2021**, *11*, 5894–5905. [CrossRef]

24. Zhang, J.; Asokan, C.; Zakem, G.; Christopher, P.; Medlin, J.W. Enhancing sintering resistance of atomically dispersed catalysts in reducing environments with organic monolayers. *Green Energy Environ.* **2022**, *7*, 1263–1269. [CrossRef]

25. Gao, F.; Tang, X.; Yi, H.; Chu, C.; Li, N.; Li, J.; Zhao, S. In-situ DRIFTS for the mechanistic studies of NO oxidation over α-MnO_2, β-MnO_2 and γ-MnO_2 catalysts. *Chem. Eng. J.* **2017**, *322*, 525–537. [CrossRef]

26. Sun, H.; Yu, X.; Guo, Y.; Deng, J.; Ge, M. Achieving efficient toluene oxidation over metal–organic framework-derived Pt/CeO_2-Co_3O_4 catalyst. *Appl. Surf. Sci.* **2022**, *591*, 153225. [CrossRef]

27. Zhang, Q.; Mo, S.; Li, J.; Sun, Y.; Zhang, M.; Chen, P.; Fu, M.; Wu, J.; Chen, L.; Ye, D. In situ DRIFT spectroscopy insights into the reaction mechanism of CO and toluene co-oxidation over Pt-based catalysts. *Catal. Sci. Technol.* **2019**, *9*, 4538–4551. [CrossRef]

28. Shi, Y.; Wan, J.; Kong, F.; Wang, Y.; Zhou, R. Influence of Pt dispersibility and chemical states on catalytic performance of Pt/CeO_2-TiO_2 catalysts for VOCs low-temperature removal. *Colloids Surf. A Physicochem. Eng. Asp.* **2022**, *652*, 129932. [CrossRef]

29. Fan, J.; Sun, Y.; Fu, M.; Li, J.; Ye, D. Modulate the metal support interactions to optimize the surface-interface features of Pt/CeO_2 catalysts for enhancing the toluene oxidation. *J. Hazard. Mater.* **2022**, *424*, 127505. [CrossRef]

30. Gao, E.; Jin, Q.; Zhang, T.; Han, L.; Li, N.; Xu, J.; Yao, S.; Wu, Z.; Li, J.; Zhu, J.; et al. Unraveling the promotional effects of K-doping on the mobility of surface oxygen species of $CoCr_2O_4$ for improved formaldehyde catalytic oxidation: The weakened metal-oxygen bond strength. *Chem. Eng. J.* **2023**, *474*, 145618. [CrossRef]

31. Yang, W.; Su, Z.A.; Xu, Z.; Yang, W.; Peng, Y.; Li, J. Comparative study of α-, β-, γ- and δ-MnO_2 on toluene oxidation: Oxygen vacancies and reaction intermediates. *Appl. Catal. B Environ.* **2020**, *260*, 118150. [CrossRef]

32. Lin, J.; Wang, X.; Zhang, T. Recent progress in CO oxidation over Pt-group-metal catalysts at low temperatures. *Chin. J. Catal.* **2016**, *37*, 1805–1813. [CrossRef]

33. Ye, J.; Zhou, M.; Le, Y.; Cheng, B.; Yu, J. Three-dimensional carbon foam supported MnO_2/Pt for rapid capture and catalytic oxidation of formaldehyde at room temperature. *Appl. Catal. B Environ.* **2020**, *267*, 118689. [CrossRef]

34. Liang, S.; Teng, F.; Bulgan, G.; Zong, R.; Zhu, Y. Effect of Phase Structure of MnO_2 Nanorod Catalyst on the Activity for CO Oxidation. *J. Phys. Chem. C* **2008**, *112*, 5307–5315. [CrossRef]

35. Ede, S.R.; Ramadoss, A.; Anantharaj, S.; Nithiyanantham, U.; Kundu, S. Enhanced catalytic and supercapacitor activities of DNA encapsulated β-MnO_2 nanomaterials. *Phys. Chem. Chem. Phys.* **2014**, *16*, 21846–21859. [CrossRef] [PubMed]

36. Xu, Z.; Mo, S.; Li, Y.; Zhang, Y.; Wu, J.; Fu, M.; Niu, X.; Hu, Y.; Ye, D. Pt/MnO_x for toluene mineralization via ozonation catalysis at low temperature: SMSI optimization of surface oxygen species. *Chemosphere* **2022**, *286*, 131754. [CrossRef] [PubMed]

37. Mo, S.; Li, J.; Liao, R.; Peng, P.; Li, J.; Wu, J.; Fu, M.; Liao, L.; Shen, T.; Xie, Q.; et al. Unraveling the decisive role of surface CeO_2 nanoparticles in the Pt-CeO_2/MnO_2 hetero-catalysts for boosting toluene oxidation: Synergistic effect of surface decorated and intrinsic O-vacancies. *Chem. Eng. J.* **2021**, *418*, 129399. [CrossRef]

38. Liu, W.; Sheng, H.; Zhu, L.; Zhang, Y.; Liu, W.; Zhao, Y.; Li, Q.; Peng, Y.; Wang, Z. The preparation of ultrastable Al^{3+} doped CeO_2 supported Au catalysts: Strong metal-support interaction for superior catalytic activity towards CO oxidation. *J. Colloid Interface Sci.* **2022**, *627*, 53–63. [CrossRef]

39. He, K. In situ DRIFTS and TPD studies on surface properties affecting SO_2-resistance of Pt/TiO_2 catalyst in low-temperature CO oxidation. *Surf. Sci.* **2023**, *734*, 122315. [CrossRef]

40. Xu, J.; Xu, X.-C.; Ouyang, L.; Yang, X.-J.; Mao, W.; Su, J.; Han, Y.-F. Mechanistic study of preferential CO oxidation on a Pt/NaY zeolite catalyst. *J. Catal.* **2012**, *287*, 114–123. [CrossRef]

41. Meunier, F.C.; Tibiletti, D.; Goguet, A.; Reid, D.; Burch, R. On the reactivity of carbonate species on a Pt/CeO_2 catalyst under various reaction atmospheres: Application of the isotopic exchange technique. *Appl. Catal. A Gen.* **2005**, *289*, 104–112. [CrossRef]

42. Zhang, T.; Xu, J.; Sun, Y.; Fang, S.; Wu, Z.; Gao, E.; Zhu, J.; Wang, W.; Dai, L.; Liu, W.; et al. Exploring the key components of Au catalyst during CO oxidation using TG-MS and operando DRIFTS-MS. *Mol. Catal.* **2023**, *547*, 113361. [CrossRef]

43. Koo, K.Y.; Jung, U.H.; Yoon, W.L. A highly dispersed Pt/γ-Al_2O_3 catalyst prepared via deposition–precipitation method for preferential CO oxidation. *Int. J. Hydrogen Energy* **2014**, *39*, 5696–5703. [CrossRef]